Available online at www.sciencedirect.com
ScienceDirect
Journal of Sound and Vibration 304 (2007) 91–109
JOURNAL OF SOUND AND VIBRATION
www.elsevier.com/locate/jsvi

Uncertainty analysis of the two-microphone method

Todd Schultz, Mark Sheplak, Louis N. Cattafesta III*

Interdisciplinary Microsystems Group, Department of Mechanical and Aerospace Engineering, University of Florida, Gainesville, FL 32611-6250, USA

Received 29 November 2005; received in revised form 25 July 2006; accepted 1 February 2007
Available online 6 April 2007

Abstract

Accurate duct acoustic propagation models are required to characterize and subsequently reduce aircraft engine noise. The boundary conditions for these models ultimately rely on accurate measurements of the acoustic impedance for candidate nacelle liners. The standard two-microphone method is widely used to estimate acoustic impedance but does not provide uncertainty estimates that are essential for data quality assessment and model validation. A systematic framework is presented in this paper to propagate the experimental 95% confidence interval uncertainty estimates in the measured quantities to the calculated acoustic impedance data using the two-microphone method for small and large input uncertainties. One method is an analytical, small-perturbation technique using multivariate statistics. This method provides useful analytical scaling information. A second Monte Carlo method is utilized to validate the analytical multivariate method. Both methods are applied to the two-microphone method for simulated data representative of sound-hard and sound-soft acoustic materials. The results indicate that for realistic experimental parameters, the uncertainty in the input measurements results in nonlinear perturbations. Therefore, the small-perturbation technique fails and the Monte Carlo method should be used to obtain uncertainty estimates. Furthermore, the nonlinear perturbations also distort the output statistical distributions of the calculated acoustic impedance and reflection coefficient, which results in significant deviation from Gaussian behavior. The distortion is a function of the acoustic impedance of the specimen itself. Finally, the Monte Carlo method is applied to experimental data for a ceramic tubular specimen and compared to the multivariate results to demonstrate the implementation and usefulness of the technique.

1. Introduction

Acoustic liners are widely used in turbofan engines to suppress engine noise. These liners provide an acoustic impedance boundary condition for modes inside the engine duct [1]. Liner design requires experimental verification of the acoustic properties of candidate configurations. The two-microphone method is a popular standardized technique for determining the normal-incidence acoustic impedance of materials [2–6]. In this method, a compression driver is mounted at one end of an acoustic waveguide or plane-wave tube, and the test specimen is mounted at the other. Two microphones are flush-mounted in the duct wall at

*Corresponding author. Tel.: +1 353 846 3017; fax: +1 353 392 7303.
E-mail address: cattafes@ufl.edu (L.N. Cattafesta III).

0022-460X/$ - see front matter © 2007 Elsevier Ltd. All rights reserved.
doi:10.1016/j.jsv.2007.02.015

two locations near the specimen to determine the incident and reflected waves. The microphone data are used to estimate the complex reflection coefficient and corresponding acoustic impedance of the test specimen.

The process of designing the experiment requires an understanding of the frequency scaling of uncertainties in microphone location, ambient temperature, etc. and how these contribute to the overall uncertainty in the reflection coefficient and acoustic impedance. Current $\frac{1}{5}$th-scale aeroacoustic impedance testing requires a frequency range of dc to 20 kHz [1]. Previous studies on the uncertainty of the two-microphone method have discussed in detail specific error sources due to uncertainties in spectral estimates [7–9] and the microphone spacing and locations [7,8,10] and have provided recommendations to minimize the respective error component. Results on the propagation of component uncertainties to the calculated reflection factor and acoustic impedance are provided in Refs. [7,8]. Authors of Refs. [7,8] use direct numerical simulations to study the effects of the component error sources on the calculated quantities, the reflection factor and the normalized acoustic impedance, but in Ref. [7] Åbom and Bodén also consider a linear Taylor-series expansion for the reflection factor. However, these efforts did not provide a systematic method to propagate the component uncertainties to the overall uncertainty in the acoustic impedance and reflection factor for experimental data. The purpose of this paper is to provide a systematic framework to accomplish this task. In particular, a frequency-dependent 95% confidence interval is estimated using both multivariate uncertainty analysis and Monte Carlo methods. The multivariate uncertainty analysis is an analytical method that assumes small uncertainties that cause only linear variations in the output quantities, but differs from classical uncertainty methods by allowing multiple, possibly correlated, components to be tracked. As long as the data reduction equation can be cast into a multivariate equation and the derivatives can be found, the multivariate uncertainty method provides a convenient way to propagate the experimental uncertainty. The multivariate technique is required because the measured data and the final output of the two-microphone method are complex variables that are treated as bivariate variables. The input covariance matrix and Jacobian are computed and propagated through the data reduction equation [11,12]. The multivariate method thus provides analytical expressions that are used to extract important scaling information, while the Monte Carlo simulations are used to account for the nonlinear perturbations of the input uncertainties observed in practice.

The paper is organized as follows. First, the two-microphone method is reviewed. A general procedure to estimate the complex uncertainty using the multivariate method is outlined followed by a brief discussion of the major error sources and their respective frequency scaling. The results of numerical simulations to illustrate the relative advantages and disadvantages of the two-microphone method and the multivariate method follow. Specifically, two impedance cases are presented, a sound-hard boundary that is representative of a high-impedance sample, and an ''ideal'' impedance sample that is representative of an optimum impedance for a ducted turbofan. Monte Carlo simulations are used to compare with the results of the multivariate method. The paper concludes with the presentation of experimental data and corresponding uncertainty estimates for a ceramic tubular specimen using the Monte Carlo and multivariate methods.

2. Two-microphone method fundamentals

A schematic of the experimental setup of the two-microphone method is given in Fig. 1. From the plane-wave assumption, the sound field inside the waveguide is described by [13,14]

$$p' = \mathrm{Re}\left(P_i\left(\mathrm{e}^{\mathrm{j}(\omega t+kd)} + R\,\mathrm{e}^{\mathrm{j}(\omega t-kd)}\right)\right), \tag{1}$$

where the $\mathrm{e}^{\mathrm{j}(\omega t+kd)}$ term represents the incident waves, the $\mathrm{e}^{\mathrm{j}(\omega t-kd)}$ term represents the reflected waves, d is the axial distance from the specimen surface, k is the wavenumber, P_i is the complex pressure amplitude of the incident wave, ω is the angular frequency, Re( ) denotes the real part of the argument, and R is the complex reflection coefficient. When dissipation and dispersion are neglected for an ideal gas, the wavenumber is given by

$$k = \frac{\omega}{c_0}, \tag{2}$$

where $c_0 = \sqrt{\gamma R_{\mathrm{gas}} T}$ is the isentropic speed of sound, γ is the ratio of specific heats, T is absolute temperature, and R_{gas} is the ideal gas constant. To account for dissipation, a complex wavenumber can be used in which the

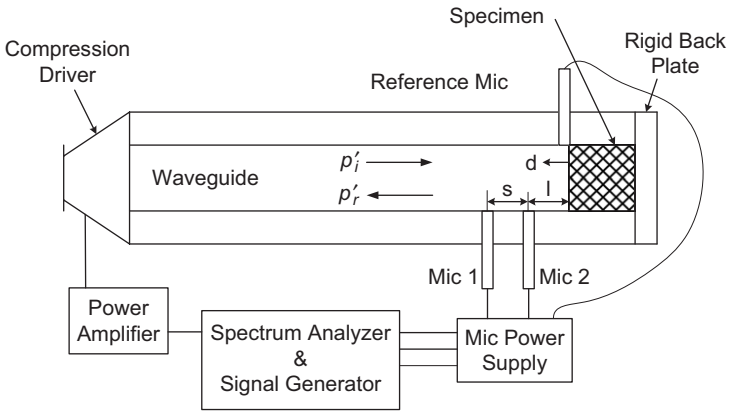

Fig. 1. Schematic of the experimental setup for the two-microphone method.

imaginary part corresponds to an attenuation coefficient, and the speed of sound is adjusted to account for dispersion [13–15]. An expression for the reflection coefficient is obtained by taking the ratio of Eq. (1) for two different axial locations and solving for R. There are two standards that provide different versions of the final data reduction equation for the reflection coefficient: ASTM E1050-98 [2] and ISO 10534-2:1998 [4]. The main difference between the two standards is the definition of the reference length, l. ISO 10534-2 defines l to be the distance from the specimen to the microphone farthest away from the test specimen, while ASTM E1050 defines l to be the distance from the specimen to the nearest microphone. In the remainder of this paper the latter definition will be used, namely

$$R = \frac{\hat{H} - \mathrm{e}^{-\mathrm{j}ks}}{\mathrm{e}^{\mathrm{j}ks} - \hat{H}} \mathrm{e}^{\mathrm{j}2k(l+s)}, \tag{3}$$

where $\hat{H} = E[\hat{G}_{12}/\hat{G}_{11}]$ is the estimated frequency response function between the two microphones, $E[\,]$ is the expectation operator, $\hat{G}_{12}$ is the estimated cross spectral density, $\hat{G}_{11}$ is the estimated autospectral density, and s is the spacing between the microphones [16]. The normalized complex acoustic impedance is computed from R

$$\xi = \theta + \mathrm{j}\chi = \frac{Z_1}{Z_0} = \frac{1+R}{1-R}, \tag{4}$$

where θ and χ are the normalized resistance and reactance, respectively, Z_0 is the characteristic impedance of the medium and Z_1 is specific acoustic impedance of the test specimen. Since R and ξ are complex quantities that are functions of another complex variable $\hat{H}$, the multivariate uncertainty analysis method is used to propagate the uncertainty. To employ the multivariate method, the data reduction equations given in Eqs. (3) and (4) must be separated into the real and imaginary parts denoted by the subscripts R and I, respectively. For R,

$$\begin{bmatrix} R_R \\ R_I \end{bmatrix} = \begin{bmatrix} \dfrac{2\hat{H}_R \cos(k(2l+s)) - \cos(2kl) - \left(\hat{H}_R^2 + \hat{H}_I^2\right)\cos(2k(l+s))}{1 + \hat{H}_R^2 + \hat{H}_I^2 - 2\hat{H}_R\cos(ks) - 2\hat{H}_I\sin(ks)} \\ \dfrac{2\hat{H}_R \sin(k(2l+s)) - \sin(2kl) - \left(\hat{H}_R^2 + \hat{H}_I^2\right)\sin(2k(l+s))}{1 + \hat{H}_R^2 + \hat{H}_I^2 - 2\hat{H}_R\cos(ks) - 2\hat{H}_I\sin(ks)} \end{bmatrix}. \tag{5}$$

In this form, the two variates of the reflection are functions of five input variates, $\hat{H}_R$, $\hat{H}_I$, l, s, and k. The frequency response function is also treated as two variates instead of a single quantity. The corresponding

form for the normalized specific acoustic impedance is

$$\xi = \begin{bmatrix} \theta \\ \chi \end{bmatrix} = \begin{bmatrix} \dfrac{1 - R_R^2 - R_I^2}{(1 - R_R)^2 + R_I^2} \\ \dfrac{2R_I}{(1 - R_R)^2 + R_I^2} \end{bmatrix}. \tag{6}$$

3. Two-microphone method uncertainty analysis

Previous studies of the error sources for the two-microphone method have focused on determining a general scaling of the error and an experimental design that minimizes such errors with the use of a Gaussian input signal. Seybert and Soenarko found that the bias error in the frequency response function due to spectral leakage can be minimized by using a small value for the bin width of the spectral analysis [9]. Spectral leakage can be eliminated by using a periodic input signal. They also found that locating the microphones too close to the specimen introduced bias and random errors that are a function of the measured coherence. To increase the coherence, the microphones should be placed close together, but the coherence will always be low when one of the microphone locations coincides with a node in the standing wave pattern. One of the most important findings was that when the value of s approaches an integer number of half-wavelengths, the error was increased dramatically. Bodén and Åbom expanded on these results and found that the bias error of the frequency response function estimate was impacted by the overall length of the waveguide, how reflective the specimen was, and the location of the microphones relative to the specimen [8]. The random error was a function of the coherence and was influenced by the value of the reflection coefficient, outside noise sources, and the value of ks. They suggest satisfying $0.1\pi < ks < 0.8\pi$ to keep the overall error low. In combination with their second study [7], they concluded that errors in the microphone locations dominated over (1) spatial averaging effects, (2) any offset the acoustic center has from its assumed location at the geometric center, and (3) any effects from the finite impedance of the microphones themselves. Other researchers have investigated the use of methods based on the use of multiple microphone locations to reduce the random error by using a least-squares method [5,17].

The results from the previous studies provide the necessary guidance to quantify and minimize component error sources that, together with the multivariate uncertainty and the Monte Carlo methods, can be used to provide 95% confidence intervals. The multivariate method propagates the uncertainty estimates through any data reduction equation [11,12,18–21] by using

$$\mathbf{s}_y = \mathbf{J}\mathbf{s}_x\mathbf{J}^{\mathrm{T}}, \tag{7}$$

where $\mathbf{s}_y$ is the sample covariance matrix of the output variable, $\mathbf{s}_x$ is the sample covariance matrix of the input variates, $\mathbf{J}$ is the Jacobian matrix for the data reduction equation, and the superscript T indicates the transpose. With the sample covariance matrix of the variable, the 95% confidence region is found from the probability statement [22]

$$\mathrm{Prob}\left((\mathbf{x} - \bar{\mathbf{x}})\mathbf{s}_x^{-1}(\mathbf{x} - \bar{\mathbf{x}}) \le \frac{v_{\mathrm{eff}}p}{v_{\mathrm{eff}} + 1 - p} F_{p,v_{\mathrm{eff}}+1-p,\alpha}\right) = 1 - \alpha, \tag{8}$$

where $\mathbf{x}$ is a vector representing the multivariate variable, $\bar{\mathbf{x}}$ is the sample mean vector, $\mathbf{s}_x$ is the sample covariance matrix of the mean, $F_{p,v_{\mathrm{eff}}+1-p,\alpha}$ is the statistic of the F distribution with p variates (two for a complex variable), $v_{\mathrm{eff}} + 1 - p$ degrees of freedom for a probability $1-\alpha$, and v_{eff} is the effective number of degrees of freedom from the measurements [21]. If the entire confidence region is not desired, the confidence level estimates of the uncertainty for the nth variate, U_n, can be computed from the equation

$$U_n = k_{\mathrm{cf}}u_n, \tag{9}$$

where u_n is the estimate of the sample standard deviation for the nth output variate (i.e., the square root of the diagonal elements of $\mathbf{s}_y$), and k_{cf} is the coverage factor given by

$$k_{\mathrm{cf}} = \sqrt{\frac{v_{\mathrm{eff}} p}{v_{\mathrm{eff}} + 1 - p} F_{p, v_{\mathrm{eff}}+1-p, \alpha}}. \tag{10}$$

The Jacobian matrix for the reflection coefficient is

$$\mathbf{J}_R = \begin{bmatrix} \dfrac{\partial R_R}{\partial \hat{H}_R} & \dfrac{\partial R_R}{\partial \hat{H}_I} & \dfrac{\partial R_R}{\partial l} & \dfrac{\partial R_R}{\partial s} & \dfrac{\partial R_R}{\partial T} \\ \dfrac{\partial R_I}{\partial \hat{H}_R} & \dfrac{\partial R_I}{\partial \hat{H}_I} & \dfrac{\partial R_I}{\partial l} & \dfrac{\partial R_I}{\partial s} & \dfrac{\partial R_I}{\partial T} \end{bmatrix}, \tag{11}$$

where, in this model, the wavenumber is treated solely as a function of temperature. The Jacobian matrix for the normalized specific acoustic impedance is

$$\mathbf{J}_\xi = \begin{bmatrix} \dfrac{\partial \theta}{\partial R_R} & \dfrac{\partial \theta}{\partial R_I} \\ \dfrac{\partial \chi}{\partial R_R} & \dfrac{\partial \chi}{\partial R_I} \end{bmatrix}. \tag{12}$$

A Monte Carlo method is also used to compute the uncertainties of the reflection coefficient and the acoustic impedance ratio. The Monte Carlo method involves assuming distributions for all of the input uncertainties and then randomly perturbing each input variable with a perturbation drawn from its uncertainty distribution [23]. The assumed distributions will be multivariate distributions if the input variates are correlated. Now, the perturbed input variates are used to compute the outputs, in this case R and ξ. This is repeated until the distribution of the output variable has converged, and then the output distributions are used to estimate the sample covariance matrix and the 95% confidence regions. A summary of the uncertainty sources is given in Table 1.

3.1. Frequency response function estimate

Estimates of the uncertainty and error sources in the frequency response function are documented in Refs. [9,16,24–27]. For this paper, two uncorrelated noise sources are assumed to affect a single-input/

Table 1
Elemental bias and precision error sources for the two-microphone method

Variable or origin	Error source	Error estimator
T	RTD accuracy	Manufacturer's specifications or calibration accuracy
	Ambient temporal variations	Minimize by conducting the test in limited amount of time
	Spatial variations	Characterize by measuring the temperature at different locations along the waveguide
	Random variations	Statistical methods
s, l	Caliper accuracy	Manufacturer's specifications or calibration accuracy
	Random variation	Statistical methods
Microphones	Spatial averaging	Minimize using microphones with a diameter much smaller than the wavelength
	Impedance change	Minimize using microphones with a diameter much smaller than the wavelength
$\hat{H}$	Phase mismatch	Correct for by using microphone switching
	Magnitude mismatch	Correct for by calibrating each microphone and microphone switching
	A/D limitations	Minimize by maximizing the significant bits
	Finite frequency resolution	Not present for a periodic random input signal
	Random error	Sample covariance matrix given in Ref. [12]

single-output system with a periodic and deterministic input signal, as described in Ref. [12]. Also from Ref. [12], the frequency response function estimate is

$$\begin{bmatrix} \hat{H}_R \\ \hat{H}_I \end{bmatrix} = \begin{bmatrix} \sqrt{\dfrac{\hat{G}_{22}}{\hat{G}_{11}\left(\hat{C}_{12}^2+\hat{Q}_{12}^2\right)}}\hat{C}_{12} \\ \sqrt{\dfrac{\hat{G}_{22}}{\hat{G}_{12}\left(\hat{C}_{12}^2+\hat{Q}_{12}^2\right)}}\hat{Q}_{12} \end{bmatrix}, \tag{13}$$

where $\hat{G}_{11}$ and $\hat{G}_{22}$ are the autospectral densities of the signals from microphones 1 and 2, respectively, and $\hat{C}_{12}$ and $\hat{Q}_{12}$ are, respectively, the co- and quad-spectral density functions (i.e., $\hat{G}_{12}=\hat{C}_{12}+\mathrm{j}\hat{Q}_{12}$). Eq. (13) is commonly called the $\hat{H}_3$ estimate. Any phase bias can be eliminated by using a switching technique, described in Ref. [12]. The final estimate of the frequency response function is computed from the geometric average of the two interchanged measurements as

$$\hat{H}=\sqrt{\frac{\hat{H}^O}{\hat{H}^S}}, \tag{14}$$

where $\hat{H}^O$ and $\hat{H}^S$ are the frequency response function between the microphones in their original and their interchanged locations, respectively.

The details of the estimate of the frequency response function for this system model are given in Ref. [12]. The sample covariance matrix for $\hat{H}_3$ and the Jacobian matrix needed to propagate the uncertainty to the averaged frequency response function are given in Ref. [12] and are summarized in Appendix of this paper. The uncertainty estimation requires an additional measurement with the pseudo-random source turned off to estimate the noise power spectral density.

The reflection coefficient's sensitivity to uncertainty in the frequency response function is described by

$$\frac{\partial R_R}{\partial \hat{H}_R}=2\frac{\cos(k(2l+s))-\hat{H}_R\cos(2k(l+s))+R_R\left(\cos(ks)-\hat{H}_R\right)}{1+\hat{H}_R^2+\hat{H}_I^2-2\hat{H}_R\cos(ks)-2\hat{H}_I\sin(ks)}, \tag{15}$$

$$\frac{\partial R_R}{\partial \hat{H}_I}=2\frac{-\hat{H}_I\cos(2k(l+s))+R_R\left(\sin(ks)-\hat{H}_I\right)}{1+\hat{H}_R^2+\hat{H}_I^2-2\hat{H}_R\cos(ks)-2\hat{H}_I\sin(ks)}, \tag{16}$$

$$\frac{\partial R_I}{\partial \hat{H}_R}=2\frac{\sin(k(2l+s))-\hat{H}_R\sin(2k(l+s))+R_I\left(\cos(ks)-\hat{H}_R\right)}{1+\hat{H}_R^2+\hat{H}_I^2-2\hat{H}_R\cos(ks)-2\hat{H}_I\sin(ks)} \tag{17}$$

and

$$\frac{\partial R_I}{\partial \hat{H}_I}=2\frac{-\hat{H}_I\sin(2k(l+s))+R_I\left(\sin(ks)-\hat{H}_I\right)}{1+\hat{H}_R^2+\hat{H}_I^2-2\hat{H}_R\cos(ks)-2\hat{H}_I\sin(ks)}. \tag{18}$$

Considering the case when $ks=n\pi$ leads to $\hat{H}=(-1)^n$. As a result, the common denominator in Eqs. (15)–(18) equals zero, resulting in a singularity so that any uncertainty in the frequency response function will result in a large uncertainty in the reflection coefficient. This result agrees with those reported in previous studies [7–9].

From Eqs. (15)–(18) it can be seen that the sensitivity to the uncertainty in $\hat{H}$ is dependent on the value of $\hat{H}$ and R. As $\hat{H}$ approaches the limiting values of zero or infinity (i.e., when one of the microphones is located at a node), or as the magnitude of R approaches the limit of unity, the sensitivity will increase. This implies that

the accurate measurement of the two extremes, sound-hard ($R = 1$) and pressure release ($R = -1$) boundaries that possess cusps in the standing wave patterns, possess the largest sensitivities to uncertainty.

3.2. Microphone locations

In this section the effects of the uncertainty of the microphone locations on the reflection coefficient are addressed. The respective sensitivity coefficients for the distance between the specimen and the closest microphone l and for the microphone spacing s are:

$$\frac{\partial R_R}{\partial l} = -2kR_I, \tag{19}$$

$$\frac{\partial R_I}{\partial l} = 2kR_R, \tag{20}$$

$$\frac{\partial R_R}{\partial s} = -2k\frac{\hat{H}_R \sin(k(2l+s)) - \left(\hat{H}_R^2 + \hat{H}_I^2\right)\sin(2k(l+s)) + R_R\left(\hat{H}_R \sin(ks) - \hat{H}_I \cos(ks)\right)}{1 + \hat{H}_R^2 + \hat{H}_I^2 - 2\hat{H}_R \cos(ks) - 2\hat{H}_I \sin(ks)} \tag{21}$$

and

$$\frac{\partial R_I}{\partial s} = 2k\frac{\hat{H}_R \cos(k(2l+s)) - \left(\hat{H}_R^2 + \hat{H}_I^2\right)\cos(2k(l+s)) - R_I\left(\hat{H}_R \sin(ks) - \hat{H}_I \cos(ks)\right)}{1 + \hat{H}_R^2 + \hat{H}_I^2 - 2\hat{H}_R \cos(ks) - 2\hat{H}_I \sin(ks)}. \tag{22}$$

The sensitivity coefficients for l and s are both directly proportional to the frequency via the wavenumber, emphasizing the difficulty of making accurate measurements at high frequency. Eqs. (21) and (22) have the same denominator as Eqs. (15)–(18), again showing that half-wavelength spacing $ks = n\pi$ should be avoided.

3.3. Temperature

The random uncertainty in the temperature measurement can be handled by using standard statistical procedures. The effects of temporal variations in the atmospheric conditions can be minimized by limiting the duration of the test. The spatial variation in the temperature of the waveguide can be characterized by measuring the temperature at various locations and computing the standard deviation of the measurements. The temperature sensor for this study is mounted on the exterior wall to avoid undesired reflections and scattering of the sound field inside the waveguide, and is found to give reliable estimate of the gas temperature if the wall is highly conductive. The total uncertainty in temperature is estimated from the root-sum-square of the individual uncertainties.

The sensitivity coefficients of the reflection coefficient with respect to temperature are computed by using the chain rule

$$\frac{\partial R_R}{\partial T} = \frac{\partial R_R}{\partial k}\frac{\partial k}{\partial T} \tag{23}$$

and

$$\frac{\partial R_I}{\partial T} = \frac{\partial R_I}{\partial k}\frac{\partial k}{\partial T}, \tag{24}$$

where

$$\frac{\partial R_R}{\partial k} = 2s\frac{-A\sin(k(2l+s)) + \dfrac{l}{s}\sin(2kl) + B\sin(2k(l+s)) - C}{1 + \hat{H}_R^2 + \hat{H}_I^2 - 2\hat{H}_R \cos(ks) - 2\hat{H}_I \sin(ks)}, \tag{25}$$

$$\frac{\partial R_I}{\partial k} = 2s\frac{A\cos(k(2l+s)) - \frac{l}{s}\cos(2kl) - B\cos(2k(l+s)) - C}{1+\hat{H}_R^2+\hat{H}_I^2-2\hat{H}_R\cos(ks)-2\hat{H}_I\sin(ks)}, \tag{26}$$

with

$$A = \left(1+2\frac{l}{s}\right)\hat{H}_R, \tag{27}$$

$$B = \left(1+\frac{l}{s}\right)\left(\hat{H}_R^2+\hat{H}_I^2\right) \tag{28}$$

and

$$C = R_R\left(\hat{H}_R\sin(ks)-\hat{H}_I\cos(ks)\right). \tag{29}$$

Eqs. (25)–(29) reveal that the uncertainty in R is approximately proportional to the microphone spacing. Reducing the spacing between the microphones will reduce the sensitivity of the uncertainty in the reflection coefficient with respect to the wavenumber and hence, the temperature. Also, Eqs. (25) and (26) possess the same singularity as the other derivatives at $ks = n\pi$.

For the case with dispersion and dissipation, the complex wavenumber is a function of the thermodynamic state (ambient temperature and pressure), the frequency, and the waveguide geometry [13,28]. The scaling of the uncertainty in R accounting for these effects is difficult to examine analytically. If dissipation and dispersion are neglected and an ideal gas is assumed, the wavenumber is given by Eq. (2) and is only a function of temperature. Thus, the derivative of the wavenumber with respect to temperature is

$$\frac{\partial k}{\partial T} = -k\frac{(\gamma R_{\text{gas}})}{2c_0^2}. \tag{30}$$

From Eq. (30) it can be seen that the uncertainty will increase with frequency via the wavenumber and that the uncertainty is inversely proportional to the square of the speed of sound.

3.4. Normalized acoustic impedance uncertainty

For the uncertainty analysis, the normalized specific acoustic impedance is treated as solely a function of the reflection coefficient. The Jacobian matrix is

$$\mathbf{J}_\xi = \begin{bmatrix} \frac{2\left((1-R_R)^2-R_I^2\right)}{\left((1-R_R)^2+R_I^2\right)^2} & \frac{-4R_I(1-R_R)}{\left((1-R_R)^2+R_I^2\right)^2} \\ \frac{4R_I(1-R_R)}{\left((1-R_R)^2+R_I^2\right)^2} & \frac{2\left((1-R_R)^2-R_I^2\right)}{\left((1-R_R)^2+R_I^2\right)^2} \end{bmatrix}. \tag{31}$$

Notice that each term has the same denominator and a singularity exists for a sound-hard boundary, $R = 1$. This situation will be studied further in the section below.

4. Numerical simulations

Much of the observations in Section 3 have been previously reported in Ref. [7–9]. The main contribution of this paper is to demonstrate how these uncertainty sources *propagate* and contribute to the overall uncertainty in R if they remain linear. It will be shown that for typical experimental situations, the uncertainties cause *nonlinear* perturbations in the reflection coefficient and acoustic impedance. In order to demonstrate the uncertainty propagation, numerical experiments on a sound-hard boundary and an "ideal" impedance sample are carried out by using the analytical method outlined in Section 3. From the results of these numerical experiments the overall uncertainty is estimated.

Table 2
Nominal values for the input parameters for the numeric simulations

Parameter	Value
l	32.1 mm
s	20.6 mm
T	23.8 °C

Time-series data are simulated by using Eq. (1) with a desired value of R, and the resulting data are processed by using the algorithms described in Section 3. The nominal values for the input parameters are given in Table 2. The numerical simulations are preformed for a single test frequency of 5 kHz ($ks = 0.60\pi$). This frequency is chosen because the uncertainties are bounded for these microphone locations. A parametric study of the effects of sensor signal-to-noise ratio (SNR) and uncertainties in temperature, microphone location, and spacing are studied in isolation assuming the perturbations remain linear. The relative uncertainties in the temperature, microphone location, and spacing are independently varied from 0.1% to 10% at a single frequency while the other uncertainties are set to zero and the input signal is noise free. The effect of the signal-to-noise ratio is studied by varying it from 30 to 70 dB while holding the other uncertainties to zero. The signal-to-noise ratio for the numerical simulations is based on comparing the power in the incident wave at a particular frequency to the power in the noise signal at that same frequency, and is kept constant across the entire bandwidth. Next, the total uncertainty in R as a function of frequency is estimated from the case with the relative input uncertainties of 0.01% and 1% for a signal-to-noise ratio of 40 dB. The estimated 95% confidence intervals are then compared to the results of the Monte Carlo simulation where 25,000 iterations are used to estimate the sample covariance matrix. All the variables are assumed to be normally distributed for the Monte Carlo simulation and the real and imaginary parts of the frequency response functions are assumed to be correlated, as shown in Ref. [12].

The simulations used either a zero-mean periodic random signal for a broadband periodic source or a sinusoid for single-frequency excitation. The sampling rate is 51.2 kHz and the bandwidth chosen for the broadband simulations is 0–20 kHz. Spectral estimation is carried out by segmenting the data into 1000 blocks each containing with 1024 samples, and using these blocks to calculate sample spectral density estimates. This yields a frequency resolution of 50 Hz. In these simulations, the microphone spacing is not designed to avoid the situation where $ks = n\pi$ or to maintain the inequality $0.1\pi < ks < 0.8\pi$ [7]. This is acceptable since the goal of the simulations is to demonstrate that the uncertainty analysis methods presented earlier capture the correct behavior. In an actual experiment, multiple microphone spacings can be used to avoid the regions where $ks \approx n\pi$.

4.1. Sound-hard sample

The first specimen studied is a sound-hard boundary. To avoid the singularity present in the data reduction and uncertainty expressions, the assumed value of the reflection coefficient is $R = 0.999$, which gives a standing wave ratio (the ratio of the maximum to the minimum pressure amplitude in the axial direction of the plane-wave tube) of greater than 60 dB. In Fig. 2, is shown the absolute uncertainty in the reflection coefficient as a function of the individual uncertainty in l, s and T at 5 kHz. In Fig. 3, is shown the absolute uncertainty in the reflection coefficient solely as a function of the signal-to-noise ratio. The results shown in Figs. 2 and 3 can be compared to determine the dominant source of uncertainty by determining which individual source causes the maximum uncertainty in the reflection coefficient. From the results in these figures it appears that the dominant source of uncertainty in the magnitude of the reflection coefficient is the random uncertainty in the frequency response function measurement for signal-to-noise ratios of 50 dB or lower. The dominant source of uncertainty in the phase of the reflection coefficient is in the measurement of the distance between the specimen and the nearest microphone. Improvements in the measurement of the reflection coefficient could be obtained from improvements in the accuracy of the frequency response function measurements (reducing the noise in the system, increasing the number of averages in the estimation) and the measurement of the distance between the specimen and the nearest microphone.

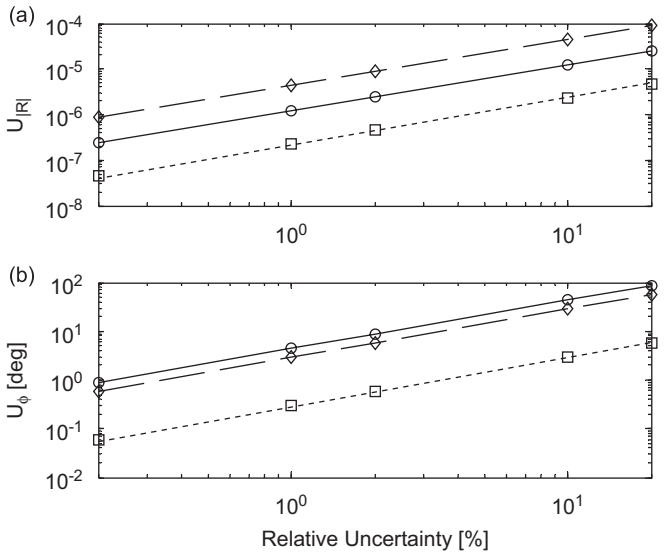

Fig. 2. Absolute uncertainty of R due to the uncertainties in l, s, and T for $R = 0.999$ at $f = 5\,\text{kHz}$. —○— l, —◇— s, - - - □ - - - T: (a) uncertainty in magnitude and (b) uncertainty in phase.

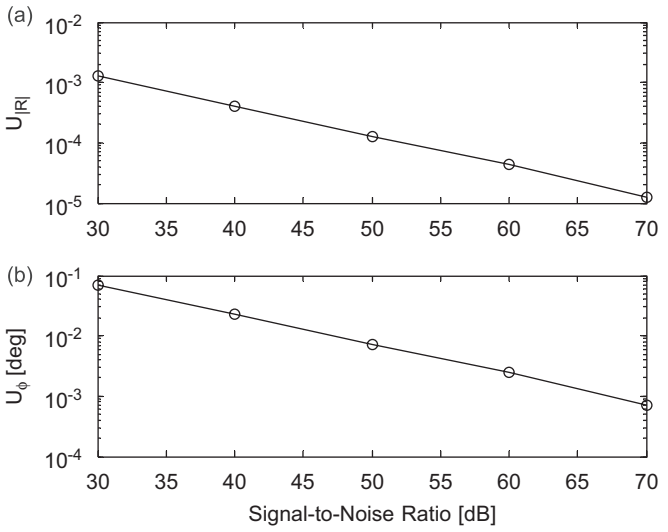

Fig. 3. Absolute uncertainty in R due to the signal-to-noise ratio for $R = 0.999$ at $f = 5\,\text{kHz}$: (a) uncertainty in magnitude and (b) uncertainty in phase.

The estimated value of the reflection coefficient with the relative uncertainty in the measurement of the microphone location, the microphone spacing, and the temperature each set to 1% and with a signal-to-noise ratio of 40 dB is given in Figs. 4(a) and (b) as a function of frequency. The uncertainty results for the multivariate method and the Monte Carlo simulation are shown in Figs. 4(c) and (d). The results form the multivariate method are in agreement with those from the Monte Carlo simulation and are within 5% for all frequencies except those corresponding to a node in the standing wave at a microphone location or the singularity where $ks \approx n\pi$; these results validate the use of the multivariate method for very small component errors. The true value only fell outside the estimated 95% confidence region for both the multivariate method and the Monte Carlo simulation five times for the magnitude, and zero times for the phase, out of the total 400 frequency bins. The results from these two methods also match at lower values of the input uncertainty, but such agreement is not universal for all acoustic materials, which is shown in the next section.

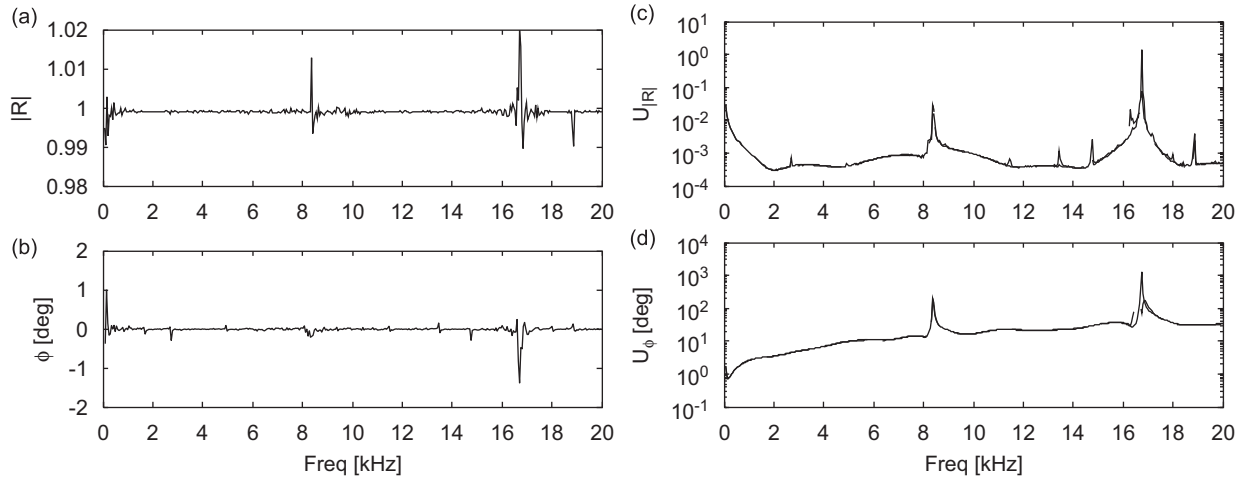

Fig. 4. Estimated value for (a) and (b) the reflection coefficient and (c) and (d) the total uncertainty for the sound hard boundary with 1% relative uncertainty for l, s, and T and 40 dB signal-to-noise ratio. Note that the peaks in the uncertainty are at frequencies 8.4 and 16.7 kHz, where $ks = n\pi$, and the frequencies where one of the microphones is at a node in the standing wave pattern are 1.6, 2.7, 4.9, 8.1, 8.2, 11.5, 13.5, 14.7, 18.0, and 18.8 kHz. ——— Multivariate method, — — Monte Carlo simulation. The two lines are indistinguishable at most frequencies.

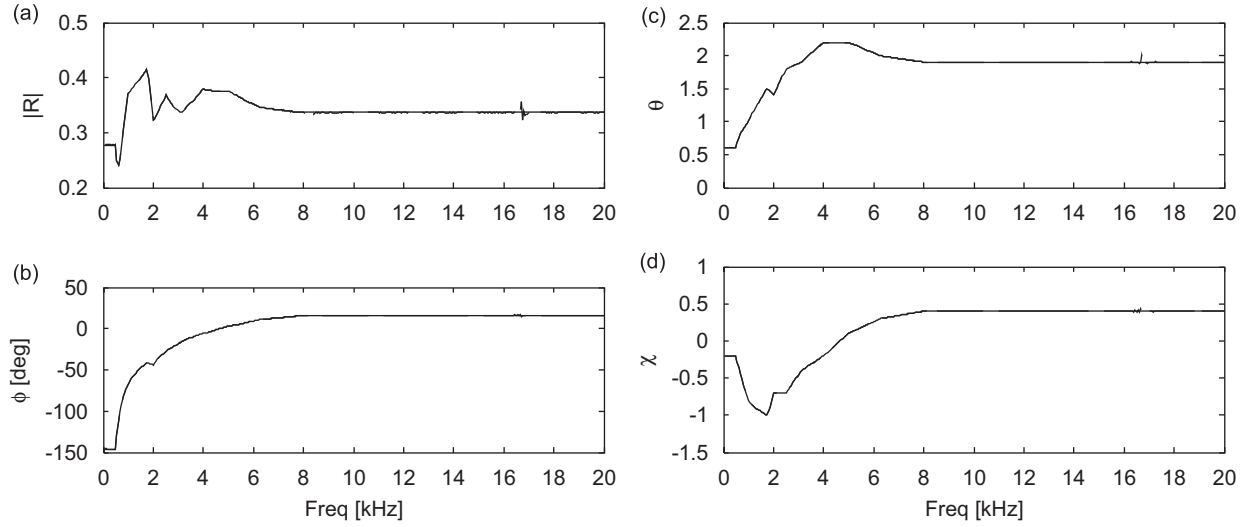

Fig. 5. Ideal impedance model and estimated values, adapted from Ref. [29], for (a) and (b) the reflection coefficient and (c) and (d) the normalized acoustic impedance. ——— Model value, — · — estimated value (40 dB signal-to-noise ratio). The two lines are indistinguishable.

4.2. Ideal impedance model

The second simulation corresponds to the ideal impedance model given in Fig. 37 of the NASA report CR-1999-209002 [29] designed by using Boeing's Multi–Element Lining Optimization (MELO) program. The data provided in the NASA report is limited to a frequency range of 500 Hz–10 kHz and is extended to the frequency range needed for this simulation by assuming that the first and last values are constant for the ranges of 0–500 Hz and 10–20 kHz, respectively. The exact reflection coefficient and normalized impedance data are given in Fig. 5. This specimen is chosen to determine the extent to which the uncertainties in a typical liner specimen scale in a similar manner to that of a sound-hard boundary. The primary distinction between

the two cases is that there are no nodes in the standing wave pattern for this impedance sample. As a result, the coherence between the two microphone signals is expected to be near unity for all frequencies assuming a reasonable signal-to-noise ratio.

In Figs. 6(a) and (b) is shown the absolute uncertainty in the reflection coefficient as a function of the individual uncertainty in l, s, and T at 5 kHz and in Figs. 6(c) and (d) is shown the absolute uncertainty in the normalized acoustic impedance. The absolute uncertainty in the reflection coefficient solely as a function of the signal-to-noise ratio is shown in Figs. 7(a) and (b), and in Figs. 7(c) and (d) the absolute uncertainty in the normalized acoustic impedance is shown. Again, the results in Figs. 6 and 7 can be compared to determine which component uncertainty dominates the uncertainty in the reflection coefficient or normalized acoustic impedance. From the results in these figures, it appears that the dominant sources of uncertainty in the magnitude and the phase of the reflection coefficient are the microphone location and spacing. In contrast to

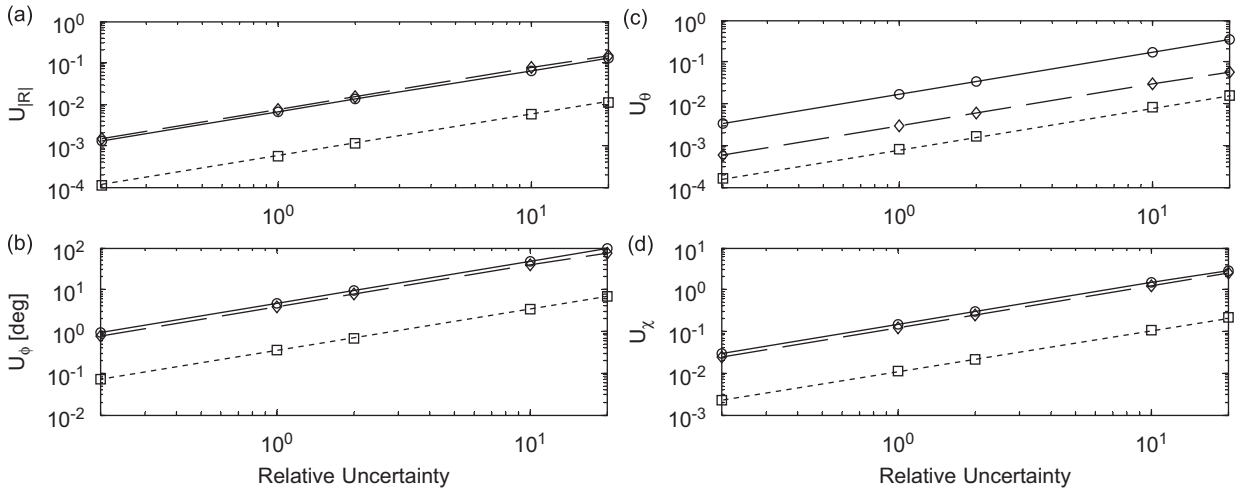

Fig. 6. Absolute uncertainty of (a) and (b) R and (c) and (d) ξ due to the uncertainties in l, s, and T for the ideal impedance model at $f = 5$ kHz. —○— l, —◇— s, - - - □ - - - T.

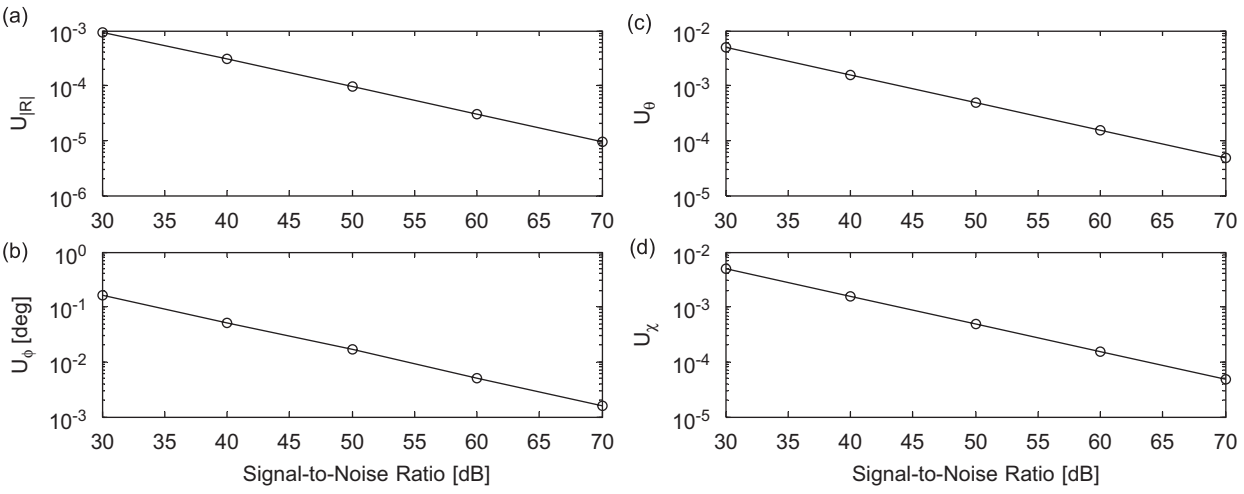

Fig. 7. Absolute uncertainty in (a) and (b) R and in (c) and (d) ξ due to the signal-to-noise ratio for the ideal impedance model at $f = 5$ kHz.

the sound-hard boundary, there is no dominating uncertainty source for the total uncertainty in the ideal impedance model data.

The estimated value of the reflection coefficient for the case with a signal-to-noise ratio of 40 dB is included in Figs. 5(a) and (b). The estimates for the normalized acoustic impedance are included in Figs. 5(c) and (d). The uncertainty results for the multivariate method and the Monte Carlo simulation are shown in Figs. 8(a) and (b) for the reflection coefficient and in Figs. 8(c) and (d) for the normalized acoustic impedance. The average percent difference between the two methods is 5% for both the magnitude and phase for the reflection coefficient for the case with only 0.01% relative uncertainty in l, s, and T and 2% for the normalized resistance and reactance. For the case with 1% relative uncertainty in l, s, and T, large differences can be seen in the estimate of the uncertainty in the magnitude of the reflection coefficient at frequencies below 6 kHz. The multivariate method does not reproduce the local minima that the Monte Carlo simulations reveal, but the multivariate method estimates are conservative for this case. The average percent difference between the results from the two methods increases to 75% for the magnitude of the reflection coefficient, 14% for the phase of the reflection coefficient, 13% for the normalized resistance, and 16% for the normalized reactance. These increases demonstrate that uncertainties in l, s, and T are causing nonlinear perturbations in both the reflection coefficient and the normalized acoustic impedance for the case with only 1% relative uncertainty. Thus, the multivariate method fails to give accurate values of the true uncertainty estimates. To increase the accuracy of the multivariate method, the multivariate Taylor series used in the derivations could be expanded to include as many terms as needed for the desired accuracy. The best option is to use numerical techniques such as the Monte Carlo simulations used in this paper to propagate the uncertainty.

The probability density function is plotted to investigate the differences between the multivariate method and the Monte Carlo simulations for large uncertainties. This is done for the normalized acoustic impedance data and for a frequency of 5 kHz where there is a large difference between the results from the two methods and by choosing this frequency complications due to the microphone spacing (see Fig. 8) are avoided. In Figs. 9(a) the confidence region contours for the case with only 0.01% relative uncertainties in l, s, and T, are shown and the corresponding results with 1% relative uncertainties are shown in Fig. 9(b). As the uncertainties become larger and cause nonlinear perturbations in the data reduction equation, the confidence region contours change from a normal distribution to an irregular "boomerang-shaped" distribution. Thus, the nonlinear effect invalidates the normal distribution assumption and the uncertainty must be found from the actual computed distribution resulting from the Monte Carlo simulation. In general, the uncertainty

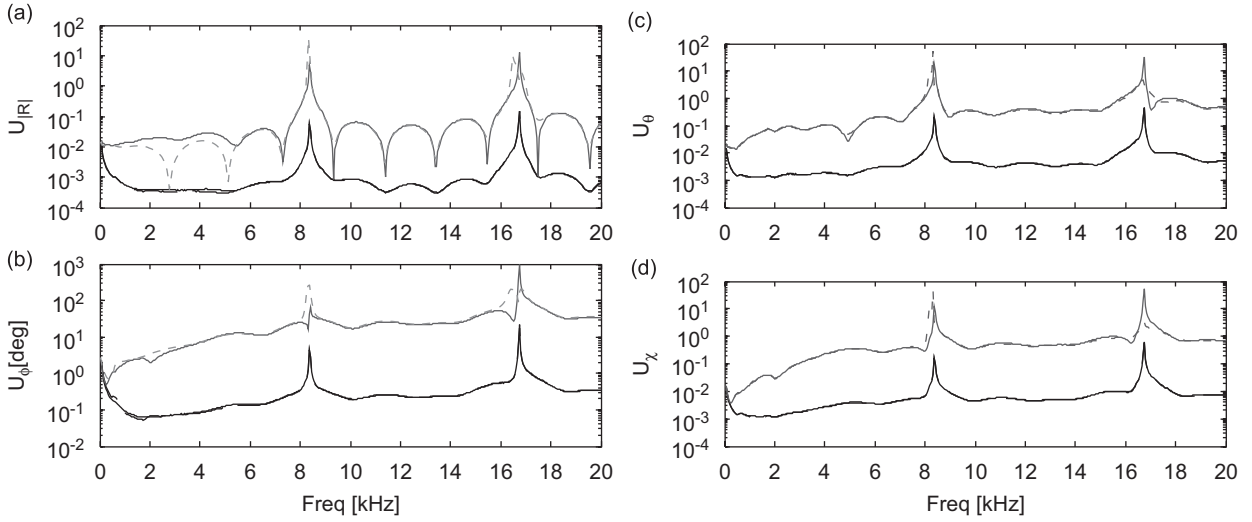

Fig. 8. Total uncertainty in (a) and (b) R and (c) and (d) ξ as a function of frequency for the ideal impedance model. The peaks in the uncertainty are at frequencies 8.4 and 16.7 kHz, where $ks = n\pi$. ——— 0.01% Multivariate method, — — 0.01% Monte Carlo simulation, –——— 1% multivariate method, — — 1% Monte Carlo simulation. The two lines for the 0.01% relative uncertainty are indistinguishable at most frequencies.

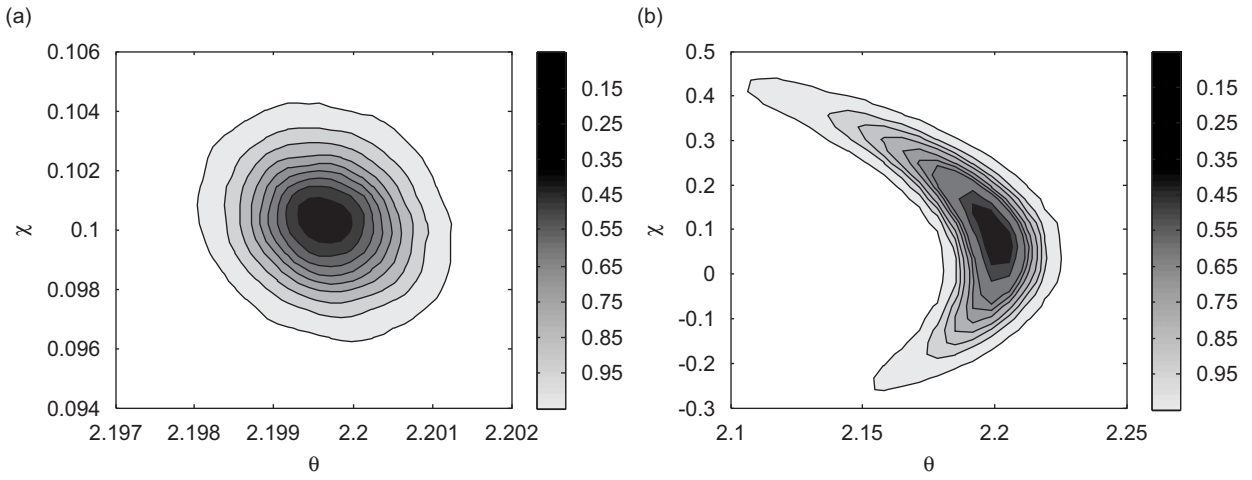

Fig. 9. The confidence region contours for the resistance and reactance for the ideal impedance model at 5 kHz with only (a) 0.01% relative uncertainties and (b) 1% relative uncertainties in l, s, and T.

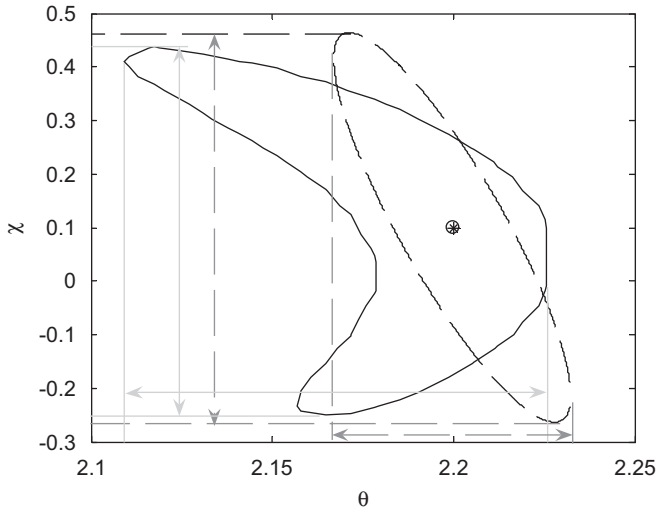

Fig. 10. Confidence region of the ideal impedance model at 5 kHz with 1% relative input uncertainty and 40 dB signal-to-noise ratio. —— Monte Carlo confidence region, — — multivariate confidence region, ○ estimated impedance, * true impedance.

cannot be approximated by the sample mean vector and the sample covariance matrix. The contour line in the joint probability density function that represents a probability of 0.95 should be found and used as the 95% confidence region estimate for the uncertainty.

To find the uncertainty in the resistance and reactance due to 1% relative uncertainty in each input variable, 25,000 iterations from the Monte Carlo simulation are used to estimate the joint probability density function which is approximated by discretizing the range of the resistance and reactance into 40 bins each, for a total of 1600 bins, and is smoothed by using a 2 bin $\times$ 2 bin kernel. Next, 100 contours of constant joint probability density are found so that it can be integrated within each contour to find the total probability within that contour. Next, the contour corresponding to 95% coverage is found via interpolation. The quoted uncertainty is then taken as the maximum and minimum values of the contour for each component, such as the resistance and reactance. For the case of the ideal impedance model with 1% relative uncertainty and a signal-to-noise ratio of 40 dB for the frequency 5 kHz, the 95% confidence region is given in Fig. 10, along with the estimated 95% confidence region from the multivariate method and the estimated and true values of the normalized

impedance. This figure illustrates the difference in the predicted uncertainty regions between the two methods and how much larger the Monte Carlo region is. The quoted uncertainty for this case is best given as a range since it is asymmetrical about the estimate. The estimate of the normalized resistance is 2.20 with a 95% confidence interval of [2.11,2.23] and the estimate of the reactance is 0.1 with a 95% confidence interval of [−0.3,0.4]. For comparison, the uncertainty estimates from the multivariate method are ± 0.03 for the resistance and ± 0.4 for the reactance.

5. Experimental data analysis

The multivariate method and the Monte Carlo method are now demonstrated on experimental data for a ceramic honeycomb test specimen with a porosity of 73%. The specimen has been demonstrated to be a linear material [5]. The specimen is 51 mm long and is encased in 12.7 mm-thick aluminum, except for the 25.4 mm by 25.4 mm test face, to prevent the loss of acoustic energy from the sides of the specimen.

5.1. Experimental setup

A schematic of the experimental setup is shown in Fig. 1. The waveguide used in this experiment has a cross-section of 25.4 mm × 25.4 mm and a usable frequency range of 0.5–6.7 kHz. The acoustic pressure signals are measured by using two Brüel and Kjær Type 4138 microphones and a Brüel and Kjær Pulse Analyzer data acquisition system. The two microphone signals are sampled at a rate of 16,384 Hz with a record length of 0.125 s and a total of 1000 spectral averages are used in the estimation. A periodic pseudo-random excitation signal is generated by the Pulse system and amplified with a Techron Model 7540 power amplifier before application to the BMS H4590P compression driver. The microphones are calibrated with a Brüel and Kjær Type 4228 Pistonphone. The excitation signal is applied, and the amplifier gain is adjusted such that the sound pressure level at the reference microphone is approximately 120 dB (ref. 20 μPa) for all frequency bins. Then the full-scale voltage on the two measurement channels of the Pulse system is adjusted to maximize the dynamic range of the data system. The excitation signal is turned off and the microphone signals are measured to estimate the noise spectra [12]. The input and output signals for the frequency response function estimation are assumed to contain uncorrelated noise and the real and imaginary parts of the frequency response function may be correlated as shown in Ref. [12]. Next, the excitation signal is turned on and the two microphone signals are recorded with the microphones in their original positions and switched positions. The time-series data are used to compute the required spectra and ultimately $\hat{H}$, R, and ξ via Eqs. (14), (3) and (4), respectively.

The ambient gas temperature is measured by using a surface-mounted platinum RTD (Omega SRTD-1). The random uncertainty is estimated from the standard deviation of 100 measurements, and the bias uncertainty is estimated by using the reported accuracy of the RTD (2 K). The total uncertainty in temperature is computed from the root-sum-square of the random and bias uncertainties.

The location of the microphone, l, and the microphone spacing, s, is measured before the experiment by using digital calipers. The measurement is repeated 45 times and the data are used to compute the estimates of the mean and standard deviation of the microphone location and spacing measurements. These are used to construct the corresponding 95% confidence intervals for the microphone location and spacing. The microphone located closest to the specimen is located 32.0 ± 0.8 mm from the specimen and the spacing between the two microphones is 20.7 ± 1.1 mm.

The uncertainty in the reflection coefficient and the measured normalized acoustic impedance is estimated by using both the multivariate method and a Monte Carlo simulation (see Fig. 11). The input distributions for l, s, and T are assumed to be independent Gaussian distributions and the input distribution for $\hat{H}$ is assumed to be a bivariate normal distribution computed from Ref. [12]. A specific form for the output distribution of the Monte Carlo simulation is not assumed as described previously at the end of Section 4. This approach is chosen because of its ability to handle the large perturbations that the uncertainties in the temperature and the microphone locations represent and to demonstrate once again that the multivariate method can only provide approximate uncertainty estimates.

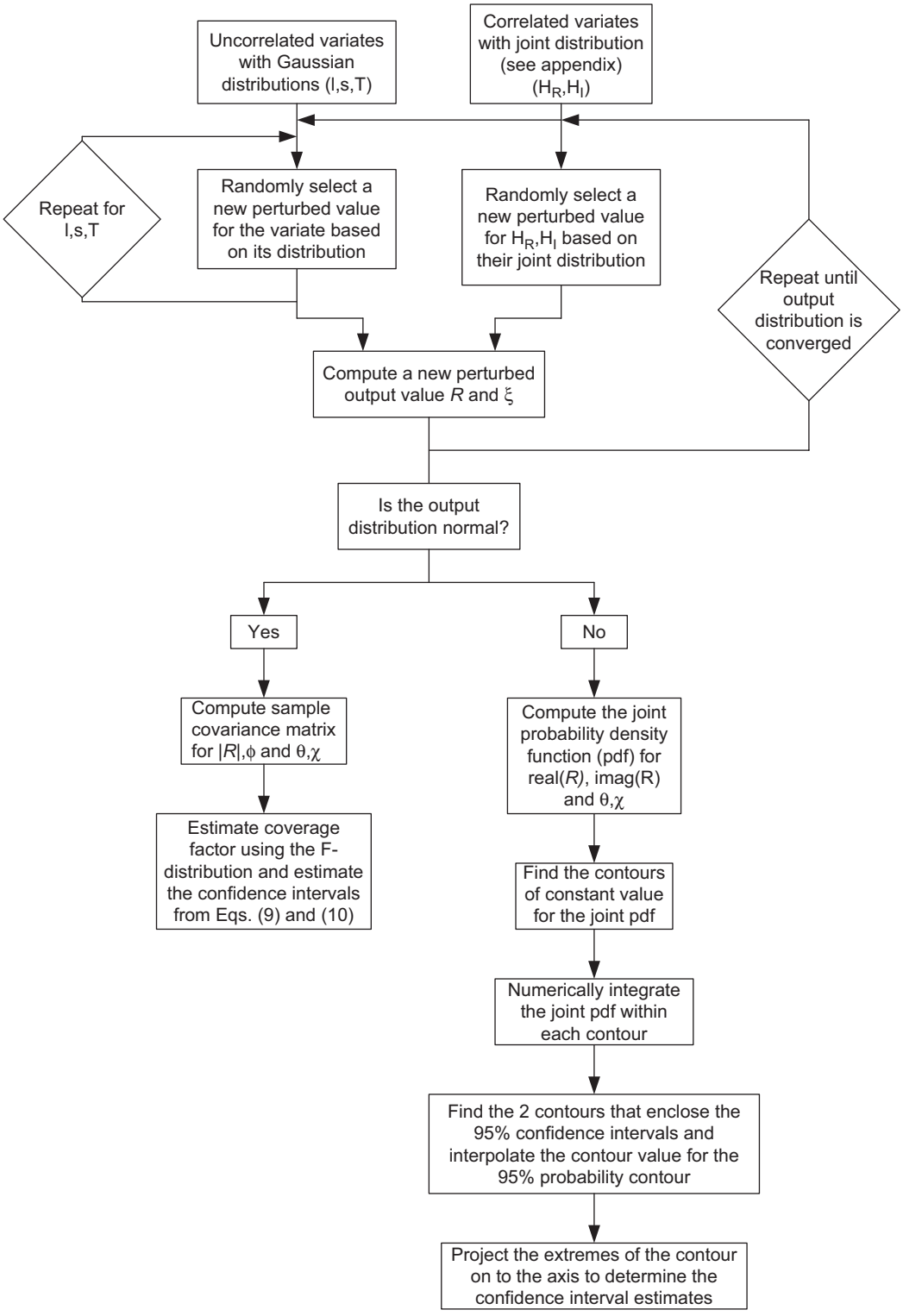

Fig. 11. Flow chart for the Monte Carlo methods. (The MATLAB computer code for this algorithm is available from the authors.)

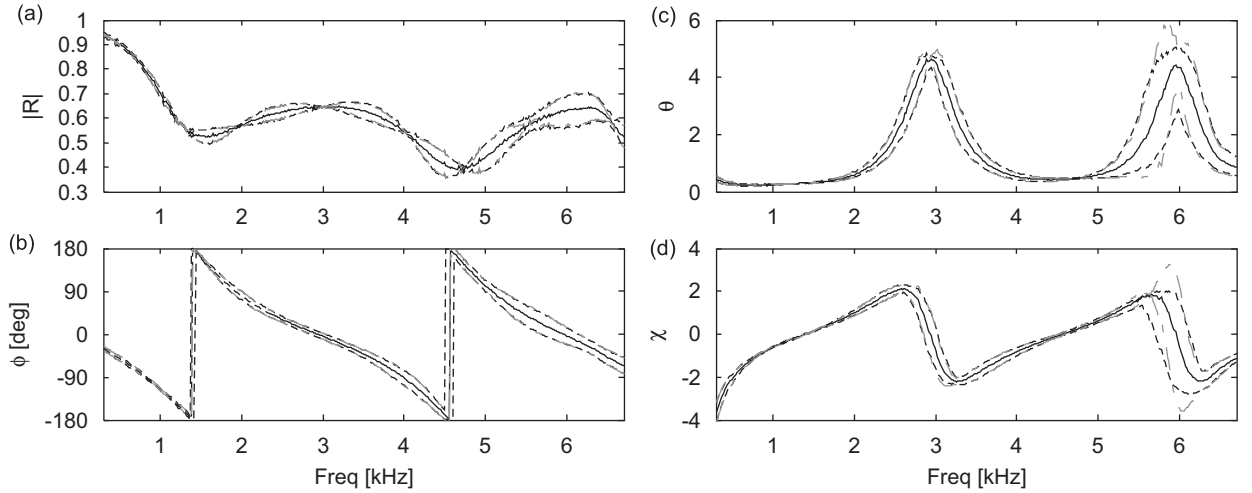

Fig. 12. The estimated (a) and (b) R and (c) and (d) ξ with uncertainty estimate for the CT73 specimen. ——— Estimate, - - - - - - - Monte Carlo uncertainty estimate, — - — - multivariate uncertainty estimate. The first uncertainty peak due to $ks = n\pi$ is at 8.4 kHz, which is beyond the frequency range of the experiment.

5.2. Results

The coherence between the two microphones for both the original and switched positions is above 0.99 for the entire bandwidth. The estimated reflection coefficient and normalized acoustic impedance are given in Fig. 12(a)–(d), together, with the corresponding uncertainty estimates. The two uncertainty estimates agree well with each other for the magnitude and phase of the reflection coefficient except around 5.55 kHz. The two uncertainty estimates for the normalized acoustic impedance only agree well with each other in a limited frequency range and exhibit large differences near 6 kHz for this case. Also, the asymmetrical uncertainty estimates at higher frequencies in the Monte Carlo simulation results are easily seen in Figs. 12(c) and (d). For example, at 5.996 kHz the normalized acoustic impedance estimate is 4.5–j0.6, but the uncertainty estimate for the normalized resistance is [3.9,5.1] for the multivariate method and [2.7,5.1] for the Monte Carlo simulation, and for the normalized reactance is [−3.6,2.4] for the multivariate method and [−2.7,1.6] for the Monte Carlo simulation.

6. Conclusions

This paper demonstrated the multivariate uncertainty analysis technique and the Monte Carlo methods for estimating the experimental uncertainties in acoustic impedance using the two-microphone method. When all of the component uncertainties are very small ($\ll 1\%$) or the specimen is sound hard, the multivariate method predictions match the results from Monte Carlo method. When the component uncertainties are at levels typically found in current experimental configurations, they are large enough to violate the assumption of linearity inherent in the multivariate method. Hence, the perturbations caused on the output are nonlinear functions of component uncertainties and the output probability distribution is not Gaussian. The distortion of the output probability distribution is thus a function of the acoustic impedance of the specimen itself. To estimate the uncertainty accurately in these situations, the actual probability density function must be estimated numerically from Monte Carlo simulations and integrated. This tends to increase the complexity of the uncertainty analysis program and requires more computation time than the multivariate method. This Monte Carlo method was demonstrated and applied to experimental data for a ceramic tubular material and the results were compared against those from the multivariate method. The Monte Carlo results demonstrated the potential for asymmetric uncertainty estimates. In general, large differences can exist between the two methods and therefore the general Monte Carlo method is recommended for accurate uncertainty estimates.

The main contribution of this paper is thus a verified systematic framework to estimate frequency dependent uncertainties in the complex reflection and normalized acoustic impedance calculations. Presumably, this tool will be useful to assess the suitability of candidate acoustic liner materials. The MATLAB® computer code for performing the two-microphone method and uncertainty analysis is available from the authors.

Acknowledgments

Financial support for the research project was provided by a NASA-Langley Research Center Grant (Grant # NAG-1-2261) monitored by Mr. Michael Jones and Mr. Tony Parrot. The first author would like to thank the NASA Graduate Student Research Program fellowship, and the National Defense Science and Engineering Graduate Fellowship administered by the American Society for Engineering Education for their financial support. All authors would like to thank Dr. James P. Hubner of the University of Alabama for introducing the topic of multivariate uncertainty analysis.

Appendix

The details of the uncertainty for the $\hat{H}_3$ estimate are provided in this appendix. These results are from Ref. [12], where a full discussion of uncertainty for frequency response functions can be found. The system model with uncorrelated input/output noise is shown in Fig. 13 and the expression for $\hat{H}_3$ was given in Eq. (13). The sample covariance matrix for $\hat{H}_3$ is

$$s_{\hat{H}_3}\left(\hat{G}_{xx},\hat{G}_{yy},\hat{C}_{xy},\hat{Q}_{xy}\right)=\begin{bmatrix} \dfrac{\hat{G}_{mm}\left(2\hat{G}_{xx}-\hat{G}_{mm}\right)}{n} & 0 & \dfrac{\hat{G}_{mm}\hat{C}_{xy}}{n} & \dfrac{\hat{G}_{mm}\hat{Q}_{xy}}{n} \\ 0 & \dfrac{\hat{G}_{nn}\left(2\hat{G}_{yy}-\hat{G}_{nn}\right)}{n} & \dfrac{\hat{G}_{nn}\hat{C}_{xy}}{n} & \dfrac{\hat{G}_{nn}\hat{Q}_{xy}}{n} \\ \dfrac{\hat{G}_{mm}\hat{C}_{xy}}{n} & \dfrac{\hat{G}_{nn}\hat{C}_{xy}}{n} & \dfrac{\psi}{2n} & 0 \\ \dfrac{\hat{G}_{mm}\hat{Q}_{xy}}{n} & \dfrac{\hat{G}_{nn}\hat{Q}_{xy}}{n} & 0 & \dfrac{\psi}{2n} \end{bmatrix}, \tag{32}$$

where $\psi=\hat{G}_{nn}\hat{G}_{xx}+\hat{G}_{mm}\hat{G}_{yy}-\hat{G}_{mm}\hat{G}_{nn}$, $\hat{G}_{mm}$ is an estimate of the power spectral density of the input noise signal, and $\hat{G}_{nn}$ is an estimate of the power spectral density of the output noise signal. The Jacobian matrix for $\hat{H}_3$ is

$$\mathbf{J}_{H_3}=\begin{bmatrix} -\sqrt{\dfrac{\hat{G}_{yy}}{\hat{G}_{xx}}}\dfrac{\hat{C}_{xy}}{2\hat{G}_{xx}\left|\hat{G}_{xy}\right|} & \dfrac{\hat{C}_{xy}}{2\sqrt{\hat{G}_{xx}\hat{G}_{yy}\left|\hat{G}_{xy}\right|^2}} & \sqrt{\dfrac{\hat{G}_{yy}}{\hat{G}_{xx}}}\dfrac{\hat{Q}_{xy}^2}{\left|\hat{G}_{xy}\right|^3} & -\sqrt{\dfrac{\hat{G}_{yy}}{\hat{G}_{xx}}}\dfrac{\hat{C}_{xy}\hat{Q}_{xy}}{\left|\hat{G}_{xy}\right|^3} \\ -\sqrt{\dfrac{\hat{G}_{yy}}{\hat{G}_{xx}}}\dfrac{\hat{Q}_{xy}}{2\hat{G}_{xx}\left|\hat{G}_{xy}\right|} & \dfrac{\hat{Q}_{xy}}{2\sqrt{\hat{G}_{xx}\hat{G}_{yy}\left|\hat{G}_{xy}\right|^2}} & -\sqrt{\dfrac{\hat{G}_{yy}}{\hat{G}_{xx}}}\dfrac{\hat{C}_{xy}\hat{Q}_{xy}}{\left|\hat{G}_{xy}\right|^3} & \sqrt{\dfrac{\hat{G}_{yy}}{\hat{G}_{xx}}}\dfrac{\hat{C}_{xy}^2}{\left|\hat{G}_{xy}\right|^3} \end{bmatrix}, \tag{33}$$

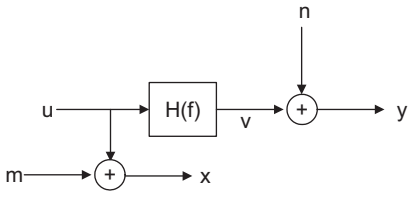

Fig. 13. System model with uncorrelated input/output noise.

where $|\hat{G}_{xy}| = \sqrt{\hat{C}_{xy}^2 + \hat{Q}_{xy}^2}$. The standard uncertainty in $\hat{H}_3$ is found by propagating the sample covariance matrix in Eq. (32) by using the propagation equation, Eq. (7), and using the techniques described in Section 3 to estimate the confidence region.

References

[1] R.E. Motsinger, R.E. Kraft, Design and performance of duct acoustic treatments, in: H.H. Hubbard (Ed.), *Aeroacoustics of Flight Vehicles: Theory and Practice, Volume 2: Noise Control*, Acoustical Society of America, New York, 1995, pp. 165–206.

[2] ASTM-E1050-98, *Impedance and Absorption of Acoustical Materials Using a Tube, Two Microphones and Digital Frequency Analysis System*, ASTM International, 1998.

[3] J.Y. Chung, D.A. Blaser, Transfer function method of measuring in-duct acoustic properties, I-theory, II-experiment, *Journal of the Acoustical Society of America* 68 (3) (1980) 907–921.

[4] ISO-10534-2:1998, *Acoustics-Determination of Sound Absorption Coefficient and Impedance in Impedance Tubes—Part 2: Transfer-Function Method,* International Organization for Standardization, 1998.

[5] M.G. Jones, T.L. Parrott, Evaluation of a multi-point method for determining acoustic impedance, *Mechanical Systems and Signal Processing* 3 (1) (1989) 15–35.

[6] M.G. Jones, P.E. Stiede, Comparison of methods for determining specific acoustic impedance, *Journal of the Acoustical Society of America* 101 (5) (1997) 2694–2704.

[7] M. Åbom, H. Bodén, Error analysis of two-microphone measurements in ducts with flow, *Journal of the Acoustical Society of America* 83 (6) (1988) 2429–2438.

[8] H. Bodén, M. Åbom, Influence of errors on the two-microphone method for measuring acoustic properties in ducts, *Journal of the Acoustical Society of America* 79 (2) (1986) 541–549.

[9] A.F. Seybert, B. Soenarko, Error analysis of spectral estimates with application to the measurement of acoustic parameters using random sound fields in ducts, *Journal of the Acoustical Society of America* 69 (4) (1981) 1190–1199.

[10] B.F.G. Katz, Method to resolve microphone and sample location errors in the two-microphone duct measurement method, *Journal of the Acoustical Society of America* 108 (5) (2000) 2231–2237.

[11] T. Schultz, *Acoustic Impedance Testing for Aeroacoustic Applications, in Mechanical and Aerospace Engineering*, University of Florida, Gainesville, FL, 2006.

[12] T. Schultz, M. Sheplak, L. Cattafesta, Multivariate uncertainty analysis and application to the frequency response function estimate, *Journal of Sound and Vibration* (2007), to appear.

[13] D.T. Blackstock, *Fundamentals of Physical Acoustics*, Wiley, New York, 2000.

[14] A.D. Pierce, *Acoustics: An Introduction to its Physical Principles and Applications*, Acoustical Society of America, Woodbury, NY, 1994.

[15] U. Ingard, V.K. Singhal, Sound attenuation in turbulent pipe flow, *Journal of the Acoustical Society of America* 55 (3) (1974) 535–538.

[16] J.S. Bendat, A.G. Piersol (Eds.), *Random Data*, Wiley, New York, 2000 (pp. 316–345, 425–431).

[17] S.-H. Jang, J.-G. Ih, On the multiple microphone method for measuring in-duct acoustic properties in the presence of mean flow, *Journal of the Acoustical Society of America* 103 (3) (1998) 1520–1526.

[18] B.D. Hall, Calculating measurement uncertainty for complex-valued quantities, *Measurement Science and Technology* 14 (2003) 368–375.

[19] B.D. Hall, On the propagation of uncertainty in complex-valued quantities, *Metrologia* 41 (2004) 173–177.

[20] N.M. Ridler, M.J. Salter, An approach to the treatment of uncertainty in complex S-parameter measurements, *Metrologia* 39 (2002) 295–302.

[21] R. Willink, B.D. Hall, A classical method for uncertainty analysis with multidimensional data, *Metrologia* 39 (2002) 361–369.

[22] R.A. Johnson, D.W. Wichern, *Applied Multivariate Statistical Analysis*, fifth ed., Prentice-Hall, Upper Saddle River, NJ, 2002.

[23] H.W. Coleman, W.G. Steele, *Experimentation and Uncertainty Analysis for Engineers*, second ed., Wiley, New York, 1999.

[24] R. Pintelon, Y. Rolain, W.V. Moer, Probability density function for frequency response function measurements using periodic signals, *Proceedings of the IEEE Instrumentation and Measurement Technology Conference*, Anchorage, AK, 2002.

[25] R. Pintelon, J. Schoukens, Measurement of frequency response functions using periodic excitations, corrupted by correlated input/output errors, *IEEE Transactions on Instrumentation and Measurement* 50 (6) (2001) 1753–1760.

[26] H. Schmidt, Resolution bias errors in spectral density, frequency response and coherence function measurements, I–VI, *Journal of Sound and Vibration* 101 (3) (1985) 347–427.

[27] A.F. Seybert, J.F. Hamilton, Time delay bias errors in estimating frequency response and coherence functions, *Journal of Sound and Vibration* 60 (1) (1978) 1–9.

[28] P.M. Morse, K.U. Ingard, *Theoretical Acoustics*, Princeton University Press, Princeton, NJ, 1986.

[29] Bielak, G.W., J.W. Premo, and A.S. Hersh, Advanced tubrofan duct liner concepts. NASA-LaRC: NASA/CR-1999-209002, 1999.